

CO Line Emission from Compact Nuclear Starburst Disks Around Active Galactic Nuclei

J. N. Armour¹ and D. R. Ballantyne¹

ABSTRACT

There is substantial evidence for a connection between star formation in the nuclear region of a galaxy and growth of the central supermassive black hole. Furthermore, starburst activity in the region around an active galactic nucleus (AGN) may provide the obscuration required by the unified model of AGN. Molecular line emission is one of the best observational avenues to detect and characterize dense, star-forming gas in galactic nuclei over a range of redshift. This paper presents predictions for the carbon monoxide (CO) line features from models of nuclear starburst disks around AGN. These small scale ($\lesssim 100$ pc), dense and hot starbursts have CO luminosities similar to scaled-down ultra-luminous infrared galaxies and quasar host galaxies. Nuclear starburst disks that exhibit a pc-scale starburst and could potentially act as the obscuring torus show more efficient CO excitation and higher brightness temperature ratios than those without such a compact starburst. In addition, the compact starburst models predict strong absorption when $J_{\text{Upper}} \gtrsim 10$, a unique observational signature of these objects. These findings allow for the possibility that CO SLEDs could be used to determine if starburst disks are responsible for the obscuration in $z \lesssim 1$ AGN. Directly isolating the nuclear CO line emission of such compact regions around AGN from galactic-scale emission will require high resolution imaging or selecting AGN host galaxies with weak galactic-scale star formation. Stacking individual CO SLEDs will also be useful in detecting the predicted high- J features.

Subject headings: accretion, accretion disks — galaxies: active — galaxies: nuclei — molecular processes — ISM: molecules

¹Center for Relativistic Astrophysics, School of Physics, Georgia Institute of Technology, 837 State Street, Atlanta, GA 30332-0430; jarmour3@gatech.edu

1. Introduction

The growth and structure of active galactic nuclei (AGN) and their effect on the development of their host galaxies are amongst the most popular and intensive areas of research in modern astrophysics. These objects are believed to consist of a central supermassive black hole (SMBH) surrounded by an accretion disk (e.g., Lynden-Bell 1969; Shakura & Sunyaev 1973). The infalling material of the disk produces the characteristic emission of the AGN. Despite this accepted universal mechanism to explain the appearance of AGN, the properties of the emission of a particular nucleus can vary greatly and are believed to be explained by the unified model of AGN, which accounts for the differences between various sub-classes of active galactic nuclei by positing the existence of extensive obscuration in the region near the AGN (e.g., Antonucci & Miller 1985; Maiolino & Rieke 1995). This obscuration is required to be anisotropic by the available evidence and is believed to be caused by material concentrated in a torus around the active galactic nucleus (Antonucci 1993).

However, multiple observations have now shown that this simple unified picture cannot hold over all redshifts and AGN luminosities. The obscured fraction of AGNs decreases with luminosity (e.g., Ueda et al. 2003; La Franca et al. 2005; Simpson 2005; Akylas et al. 2006; Hasinger 2008; Treister et al. 2008; Tueller et al. 2008; Draper & Ballantyne 2011) and seems to increase with redshift (e.g., Ballantyne et al. 2006; Treister & Urry 2006; Hasinger 2008). Well-sampled monitoring of some local Seyfert galaxies show rapid changes of X-ray obscuring columns, indicating a dynamic and clumpy medium (e.g., Risaliti et al. 2010). Global population synthesis models that include both X-ray and optical/near-IR constraints indicate that the unified model seems to hold only for $z \lesssim 1$ (Draper & Ballantyne 2011). These results all point to a scenario where there are different origins for the AGN obscuration that depend on the redshift and luminosity of the central engine (e.g., Ballantyne et al. 2006; Hasinger 2008).

A possible origin for the obscuring torus in $z < 1$ Seyfert galaxies is a nuclear starburst disk (e.g., Wada & Norman 2002; Ballantyne 2008; Wada et al. 2009) — compact ($\lesssim 100$ pc) regions of strong star-formation that, through a combination of radiation pressure and supernova feedback, can potentially inflate an optically thick structure and obscure the central AGNs. Indeed, simple 1-D analytic models (Ballantyne 2008) showed an AGN could be both obscured and fueled by a pc-scale ultra-compact starburst embedded in a larger nuclear starburst disk. Due to the competition for gas between star-formation and accretion, this model could only obscure Seyfert galaxies, but these are just the AGNs that dominate the hard X-ray background (e.g., Ueda et al. 2003; La Franca et al. 2005; Draper & Ballantyne 2010). Thus, it is useful to pursue the possible observational signatures of the nuclear starburst model that can be tested with the large multiwavelength AGN samples produced

by the deep X-ray surveys (e.g., Xue et al. 2011). To that end, Ballantyne (2008) discussed strategies to detect these starburst disks at mid-infrared and radio wavelengths, leading Pierce et al. (2011) to uncover evidence for the predicted levels of star-formation in radio-stacks of $z < 1$ X-ray selected AGNs.

The greatest difficulty in observationally testing the nuclear starburst disk model is separating out its emission from the AGN and the host galaxy. The high angular resolution allowed by radio interferometric observations therefore seems to be the most promising technique for further investigation. With the ongoing construction of the Atacama Large Millimeter/Submillimeter Array (ALMA), capable of reaching an angular resolution of 5 milliarcsec at 650 GHz, it is therefore interesting to consider the molecular line properties of the nuclear starburst disk models. The region within several dozen parsecs of an AGN and its central supermassive black hole is known to contain a wealth of dense and relatively warm gas (e.g. Scoville et al. 1991; Hsieh et al. 2008; Wada et al. 2009; Papadopoulos et al. 2010a). These conditions of relatively high density ($n_{H_2} \geq 10^{3-4} \text{ cm}^{-3}$) and high pressure favor the creation of significant quantities of molecular gas (e.g. Pelupessy et al. 2006). It is well-known that star formation occurs solely in molecular gas (e.g. Fukui & Kawamura 2010; Schrubba et al. 2011). For reasons outlined in a variety of sources (e.g. Dickman et al. 1986; Fukui & Kawamura 2010), carbon monoxide (CO) is the molecule most often used to probe regions of molecular gas. Despite the importance of CO lines as an observational tool, the likelihood of the existence of large quantities of molecular gas in this situation, and the possibility that molecular gas could constitute a large portion of the obscuring torus, theoretical models of the molecular emission of the torus are fairly uncommon (see Wada & Norman 2002; Wada et al. 2009; Pérez-Beaupuits et al. 2011 for examples of these simulations).

In this work, the models of Ballantyne (2008) are combined with RATRAN (Hogerheijde & van der Tak 2000), a radiative transfer code, to estimate the CO line emission from these objects. Following this procedure, CO spectral line energy distributions (SLEDs) are created, and brightness temperature ratios calculated. Section 2 contains the descriptions of the nuclear starburst disk model, the molecular mass fraction model, and RATRAN. Section 3 conveys our central results and discusses their significance and physical origin, while also comparing these results to observations of starburst and AGN host galaxies. In Section 4, the findings of this work are compared with the conclusions of similar simulations, and the possibility for the detection of AGN-obscuring starburst disks is explored. Finally, in Section 5, concluding remarks and analysis are presented.

A Λ -dominated cosmology is assumed in this paper, when necessary. The following parameters are used: $H_0 = 71 \text{ km s}^{-1} \text{ Mpc}^{-1}$, $\Omega_\Lambda = 0.73$, and $\Omega_m = 0.27$ (Spergel et al. 2003; Spergel et al. 2007).

2. Calculations

2.1. Review of the Starburst Disk Model

The nuclear starburst disks are taken from the models of Ballantyne (2008), which are based on the one-dimensional, analytic model of Thompson et al. (2005). A short elucidation of the central tenets and assumptions of this model will be presented here.

The material of the disk is assumed to be a single phase medium. The various properties of the gas are calculated for discrete values of the distance, r , from the central SMBH. The black hole mass is used to calculate the velocity dispersion of the stars in the galactic bulge, σ , according to the $M_{BH}-\sigma$ relationship (Ferrarese & Merritt 2000; Gebhardt et al. 2000; Tremaine et al. 2002). The gas is modeled as rotating at the Keplerian frequency at all radii in response to a gravitational potential composed of the sum of a point mass potential for the central black hole and the potential of an isothermal sphere to represent the galactic bulge. Star formation is unresolved but calculated locally by assuming that the star formation rate behaves so as to maintain a Toomre’s parameter of one, implying that the gas is locally marginally stable against self-gravity (i.e. $Q = \kappa_{\Omega} c_s / \pi G \Sigma_g = 1$, where κ_{Ω} is the epicyclic frequency, Ω is the Keplerian frequency, Σ_g is the surface density of gas, and c_s is the sound speed). From this assumption, the density, ρ , may be explicitly calculated as a function of the Keplerian frequency, Ω . The vertical support of the disks results from the feedback of the star formation. The radiation pressure of the infrared emissions given off by the dust forms the primary means by which this support is achieved. Accretion is assumed to occur by means of a global mechanism for the shedding of angular momentum. The process is assumed to allow the in-falling gas to achieve a radial velocity, v_r , equal to a constant fraction, m , of the speed of sound. The input parameters of this model are the mass of the central black hole M_{BH} , the accretion efficiency parameter m , the gas fraction f_{gas} , the outer radius of the disk R_{out} , and the dust-to-gas ratio d_{dtg} . The models use the dust opacities taken from the work of Semenov et al. (2003) with a density of 10^6 cm^{-3} and normal, homogeneous, and spherical grains. Calculations were then undertaken for all permutations of the input parameters, as detailed in Ballantyne (2008).

In order to model the nuclear regions of AGN host galaxies, the nuclear starburst disks must be capable of feeding the AGN, in addition to providing the required obscuration (Thompson et al. 2005; Ballantyne 2008, Section 2.1). Because of this requirement, the advection timescale, $\tau_{adv} = r/v_r$, must be less than the star formation timescale, $\tau_* = 1/(\eta\Omega)$, where η is the star formation efficiency. These considerations allow one to select the models most likely to fuel and obscure the central AGN by considering whether a region exists within the model that meets the following criteria: 1) a mid-plane temperature greater than

900 K and 2) a star formation rate greater than 10% of the rate at R_{out} . The first criterion ensures that the gas temperature reaches the dust sublimation temperature, creating a severe vertical opacity gradient. The second allows for the exclusion of models that only marginally surpass the first criterion but are still largely incapable of the obscuration required by the unified model of AGN. Those models that met both requirements were judged to contain a parsec-scale starburst capable of obscuring the central AGN. Models satisfying neither requirement were found to lack an obscuring parsec-scale starburst region. The models that failed to achieve a parsec-scale starburst had significantly lower temperatures than the starburst disk models, usually in the range of several tens of Kelvins and occasionally rising to as high as 200 K. In total, approximately 41% of the models tested met the starburst criteria (Ballantyne 2008, Section 2.2). Starburst disks were produced by sets of parameters throughout the parameter space. However, generally speaking, increasing values of all of the parameters, except the outer radius, were found to be most conducive to producing a potentially obscuring starburst. The trend seen in R_{out} indicates that smaller outer radii create conditions more amenable to obscuring starbursts (See Ballantyne 2008, Figure 3). All models, regardless of classification, were found to be high density and high pressure environments, which, as mentioned in Section 1, are conditions favoring the formation of large quantities of molecular gas.

In order to utilize the RATRAN program, a method of determining the molecular mass fraction in each annulus of the disk was needed. The densities at which molecular gas dominates over the atomic phase have been found to be relatively modest (i.e. approximately 100 cm^{-3}) compared to the densities present in the nuclear starburst disk models offered here (e.g., Solomon & Wickramasinghe 1969; Solomon & Vanden Bout 2005; Gnedin et al. 2009). Also, it has been shown that the formation rate of molecular hydrogen drops to essentially zero for temperatures above approximately 1000 K, and collisional destruction eliminates any remaining H_2 in the area (Cazaux & Tielens 2004; Pelupessy et al. 2006). As mentioned above, the nuclear starburst disk model predicts extensive star formation in these high temperature regions, as well. Because of the very high densities present in the disk models, ranging from approximately 500 cm^{-3} at R_{out} to $> 10^9 \text{ cm}^{-3}$ at the innermost radius of the disk, the molecular mass fraction, $f_m(r)$, was set to unity for regions of the disk with temperatures less than 900 K and to zero for the remaining portions of the disk¹. The temperature, T , is taken directly from the mid-plane temperature of the nuclear starburst disk models. After the molecular mass fraction is calculated, it is used to find the number

¹A more complicated molecular mass fraction recipe based on the static model of Pelupessy et al. (2006) was employed to test this scenario, and similar results were found. The molecular mass fractions of the annuli of the disks were found to lie between 0.96 and 1.0 for all of the models analyzed.

density of molecular hydrogen from the density of the nuclear starburst disk model by assuming that all of the gas is hydrogen. We then use a constant factor of $n_{CO}/n_{H_2} = 10^{-4}$ to determine the number density of carbon monoxide. This value is frequently used as the upper limit on CO abundance (Klemperer 2006).

2.2. Molecular Line Emission

With the properties calculated in section 2.1, we employ the RATRAN code written by Hogerheijde & van der Tak (2000) to calculate the line emission of the disks. We use the one-dimensional (spherically symmetric) form of the code. For a review of the assumptions and techniques of this program, one may see Hogerheijde & van der Tak (2000).

The inputs of the RATRAN code are taken from the nuclear starburst disk models and the molecular mass fraction scheme detailed in Section 2.1. We assume that the gas at each radius, r , is well-mixed with the dust and, thus, that the molecular gas kinetic temperature is equal to the mid-plane temperature. Furthermore, we set the dust temperature equal to this value because of the high density involved in the nuclear starburst disk models. We approximate the turbulent line width by the local speed of sound, which is calculated by $c_s = \sqrt{P/\rho}$, where c_s is the speed of sound and P and ρ are the local pressure and density from the nuclear starburst disk model. The Doppler broadening parameter, b , is calculated as $b = (2\sqrt{\ln(2)})^{-1}c_s$. The radial velocity is also included in the inputs for the RATRAN calculation and is calculated as follows: $v_r = mc_s$, as described in Section 2.1 and Ballantyne (2008).

As the nuclear starburst disk models depend explicitly on the absorption and emission of dust to explain the vertical support of obscuring disks, a dust opacity is included in the RATRAN calculation. As mentioned above, Ballantyne (2008) used the Semenov et al. (2003) Rosseland mean opacity curve. However, for the RATRAN code, we require a frequency-dependent opacity. Therefore, we include a broken power law dust opacity based on the work of Pollack et al. (1994) with the following form: $\kappa \propto \lambda^{-\beta}$, where β is the dust opacity spectral index. Semenov et al. (2003) reference this work, utilize the same distribution of dust components, and employ similar techniques to calculate the properties desired. The wavelengths of the emission of the lowest seventeen rotational lines of CO range from 2.6 mm to approximately 153 μm . Table 4 of Pollack et al. (1994) includes spectral indices for wavelengths between 650 μm and 2.3 mm for a wide variety of models of dust composition. We employ these indices for the wavelength range over which they apply. We then measure indices for the range between 100 μm and 650 μm from Figures 2b and 2c of Pollack et al. (1994). To attain self-consistency with the Ballantyne (2008) calculations, we

use spectral indices for spherical particles composed of segregated materials. Segregation in the Pollack et al. (1994) model corresponds to the condition of homogeneity in the Semenov et al. (2003) model, namely, that the dust particles are composed of a single constituent, rather than being a conglomeration of all the substances constituting dust. Also, for the sake of consistency, we set the dust opacity equal to zero for the regions in which the mid-plane temperature exceeds the dust sublimation temperature. We select a particle radius of $3 \mu m$, well within the size distribution of Semenov et al. (2003). Armed with these meditations, we select a dust model with a temperature of 700 K for the nuclear starburst disk models that achieved a parsec scale starburst or are borderline cases. A dust model of temperature 100 K is used for models that did not meet either criterion. Lastly, the opacities in Table 4 of Pollack et al. (1994) are given in terms of total disk mass. However, the RATRAN program requires that they be in terms of total dust mass. Thus, the following simple conversion is made: $\kappa_{M_{dust}} = \kappa_{M_{tot}} \times (M_{tot})/(M_d) = \kappa_{M_{tot}}(\delta_{gtd} + 1)$, where M_{dust} is the total mass of dust, M_{tot} is the total mass of the disk, and δ_{gtd} is the absolute value of the gas-to-dust ratio. Assuming a local ISM value for the gas-to-dust ratio of 150 (Draine & Lee 1984; Young & Scoville 1991), the absolute value of the gas-to-dust ratio, δ_{gtd} , is related to the dust-to-gas ratio parameter of the Ballantyne (2008) disk models, d_{dtg} , as follows : $\delta_{gtd} = 150/d_{dtg}$. The spectral indices and opacities used in our calculations are summarized in Table 1. The number of channels and the channel width used for the RATRAN calculations are 8000 and 0.05 km s^{-1} , respectively, well within the capabilities of ALMA (Schieven 2011; Vila Vilaro 2011).

Following the completion of the RATRAN program, the brightness temperature maps produced are analyzed using the Miriad software package (Sault et al. 1995). In particular, dust emission is removed from the line images by subtracting the first channel from all the subsequent channels for each image. The images are then convolved to a beam with a full-width at half maximum (FWHM) , θ , appropriate for ALMA given by the following equation: $\theta = (76)/(D\nu_{obs})$ arcsecs, where D is the maximum baseline of the configuration used in kilometers and ν_{obs} is the frequency at which observations are being made in GHz (Schieven 2011). For our calculations, we use a value of $D = 0.125 \text{ km}$, the maximum baseline for the most compact configuration available. Following convolution to the desired spatial resolution, the velocity-integrated intensity, I_{CO} , is found using the Miriad *moment* function. The velocity-integrated intensity is then multiplied by the source surface area to get the luminosity in $\text{K km s}^{-1} \text{ pc}^2$, L'_{CO} :

$$L'_{CO} = 4\pi \left((R_{out})^2 - (R_{in})^2 \right) I_{CO}, \quad (1)$$

where R_{in} and R_{out} are the inner and outer radii of the disk, respectively, and have units of parsecs and I_{CO} has units of K km s^{-1} . R_{in} is, generally, two to three orders of magnitude

Table 1. The spectral indices and normalizations for the power law dust opacity models

Model Type	$\beta(100 - 650\mu m)$	$\kappa(650 \mu m)$ ($\text{cm}^2 \text{g}^{-1}$)	$\beta(650 - 2700\mu m)$	$\kappa(1 \text{ mm})$ ($\text{cm}^2 \text{g}^{-1}$)
Starburst	1.83	3.7×10^{-2}	0.98	2.4×10^{-3}
Failed	2.73	7.1×10^{-2}	1.46	3.8×10^{-3}

Note. — Given here are the values for the spectral indices and normalizations used in the dust model detailed in Section 2.2. A broken power law, $\kappa \propto \lambda^{-\beta}$, is employed with one index serving for wavelengths between 100 and 650 μm and a second for wavelengths between 650 μm and 2.7 mm. The opacity power law normalizations are given for 650 μm and 1 mm. Note that the opacity normalization constants are given in terms of total disk mass, as detailed in the text.

smaller than R_{out} and, thus, was neglected in all computations. This luminosity was then converted into conventional units and used to find a flux as follows:

$$S_{line} = \frac{2k_B\nu_o^3}{D_L^2 c^3} L'_{CO}, \quad (2)$$

where D_L is the luminosity distance, k_B is the Boltzmann constant, c is the speed of light, and ν_o is the rest frequency (Papadopoulos et al. 2010a; equation 5).

3. Results

Using equations 1 and 2, brightness temperature ratios and CO spectral line energy distributions (SLEDs) are calculated for eighteen nuclear starburst disk models (see Table 2). The particular models chosen are selected to sample the parameter space of the nuclear starburst disk model widely enough that the variation of the CO emission with the input parameters can be discerned. The set of models analyzed here includes an equal number of failed and starburst cases.

3.1. The CO SLED from an Ultra-Compact Starburst

The solid black line in Figure 1 shows an example flux SLED produced by an ultra-compact starburst with an outer radius of 250 pc at $z = 0.8$, a typical redshift for the obscured Seyfert galaxies that dominate the X-ray background (e.g., Ueda et al. 2003). The input parameters of this starburst model are listed in Table 2, but its flux SLED shape and magnitude are typical for all the studied starburst models. The flux SLED shows two nearly symmetric features: a strong emission bump peaking at $J_{Upper} \approx 6-7$, and a deep absorption trough that reaches a minimum at $J_{Upper} \approx 14-15$. To understand the origin and physics behind these features we consider the flux SLEDs of the disk truncated at various radii. The red, dotted line with open triangles shows the SLED produced from only the inner 200 pc of the disk and is very similar to the total SLED, albeit with somewhat less absorption. In contrast, the SLED from the inner 50 pc of the disk (the red, dotted line with open pentagons) shows a significantly different shape with both the emission and absorption peaks shifted to higher values of J_{Upper} , indicating significant amounts of highly excited CO consistent with the high temperature and pressures predicted in this region of this disk (e.g., Ballantyne 2008). The density and temperature continues to rise culminating in a significant burst of star-formation in the inner 10-pc of the disk. The CO flux SLEDs from the inner 1.4, 2.5 and 6.3 pc of the starburst disk are also shown in Figure 1, but they all overlap and

have line fluxes close to zero at all values of J_{Upper} , indicating that these regions produce a featureless blackbody continuum, as expected for an optically thick mixture of dust and gas.

Figure 1 shows that the innermost portions of the ultra-compact starburst disk do not contribute substantially either to the emission or the absorption features seen in the final CO SLED from the entire disk. Recall that the densities in these models are universally high ranging from $\sim 500 \text{ cm}^{-3}$ at the outer radius to $\sim 10^9 \text{ cm}^{-3}$ in the innermost portions of the disk (e.g., Thompson et al. 2005; Ballantyne 2008). The fact that the critical densities of CO lines tend to be fairly low with respect to most of the densities in the disk means that CO should be fairly well excited throughout the disk. Therefore, we find that, overall, the disk acts similarly to a star: there is a hot and dense central region that produces a blackbody continuum which then must propagate through a large column of material with a steep density and temperature gradient. Intervening molecular gas, being always cooler than the gas interior to it, will absorb the higher- J_{Upper} lines while still emitting substantially at the lower- J_{Upper} line because of the relatively low critical densities of CO lines. The final CO SLED will therefore have both emission and absorption features due to the unique strong density and temperature profiles predicted by the ultra-compact starburst disk model. The emission lines highlight the excited nature of the outer molecular layers, while the absorption features indicate the presence of the hot, high-pressure center that is buried deep inside the disk.

The above physical reasoning predicts that there will not be strong differences in the CO SLEDs predicted by starburst models and those that failed to produce a pc-scale burst because the density profiles of both classes are similar. However, although the innermost portions of the disk may not contribute substantially to the total flux in any given line, they must affect the energy balance of the disk, as the failed models (by definition) do not achieve the large temperatures found in the inner regions of the starburst models. Therefore, we expect, and the data confirm (see below), that the CO SLEDs from failed models are shifted to lower J_{Upper} and are less luminous than ones produced by ultra-compact starbursts.

Finally, we emphasize that these calculations assume spherical symmetry, so the lines-of-sight always pass through the ‘edge’ of the starburst disk, and will therefore observe the maximum of the radiative transfer effects. Other, more realistic, lines-of-sight may predict weaker emission and absorption features in the SLED. This will be the subject of future work.

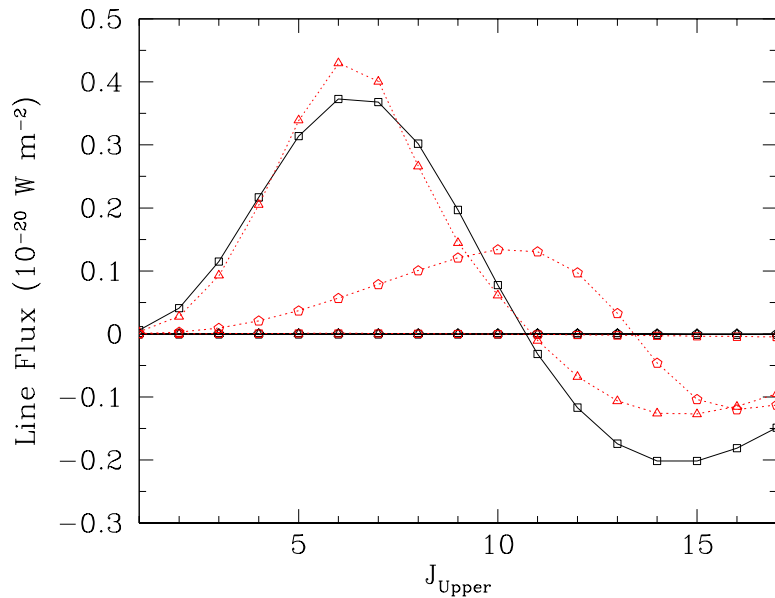


Fig. 1.— CO flux SLEDs (at $z = 0.8$) showing the contributions to the SLED from different portions of a nuclear starburst disk (see marked starburst model in Table 2). The black, solid line with square markers is the flux SLED of the entire model with an outer radius of 250 parsecs. The red, dotted line with triangles is the SLED of the inner 200 pc of the disk model. The red, dotted line with pentagons is the SLED for the region with an outer radius of 50 pc. The contributions to the SLED from the inner 1.4, 2.5 and 6.3 pc all lie along the zero flux line. Thus, much like a star, the outermost regions of the disk determine the overall shape of the flux SLED, while the innermost and hottest portions of the disk affect the magnitude of the SLED.

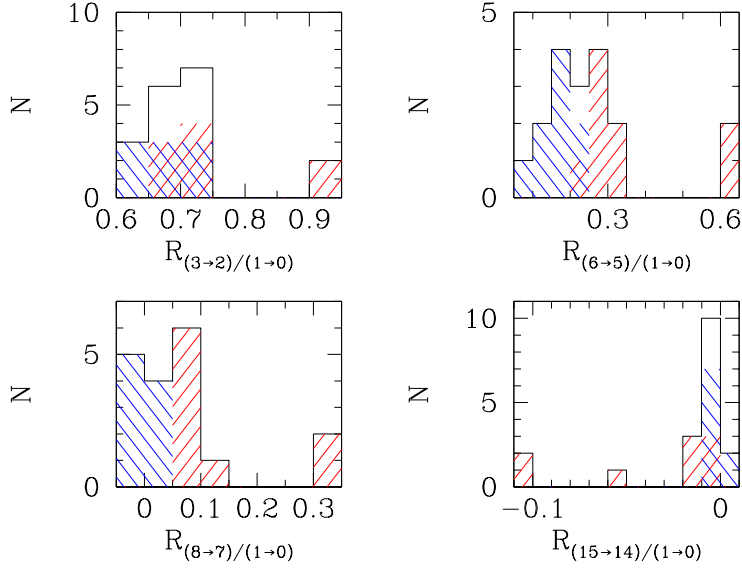


Fig. 2.— Histograms of four brightness temperature ratios for the eighteen models analyzed in this work. The distribution of ratios for the starburst models with pc-scale bursts is shaded with right-leaning (red) diagonal lines. The distribution for the failed models is marked by left-leaning (blue) lines. Note that the starburst models generally have higher values for the brightness temperature ratios for lines in which most models have not fallen into absorption. For lines in which the majority of models show absorption, starburst-classified models tend to have stronger absorption. Note also that the separation between the distributions of failed and starburst models tends to increase from the histogram of $R_{(3\rightarrow 2)/(1\rightarrow 0)}$ in which a great overlap exists to the distribution for $R_{(8\rightarrow 7)/(1\rightarrow 0)}$ in which no overlap between the two classes occurs. For ratios involving the very highest lines explored, such as $J = 15 \rightarrow 14$, little separation occurs because most models show little emission or absorption at these high lines. If the nuclear starforming region can be resolved, these ratio differences between the two model classes could be used to determine if ultra-compact, obscuring starbursts exist in the observed galaxies.

3.2. Distribution of CO SLED Properties

Turning now to the SLED properties of the eighteen analyzed models, Figure 2 displays histograms of four brightness temperature ratios, $R_{(3\rightarrow 2)/(1\rightarrow 0)}$, $R_{(6\rightarrow 5)/(1\rightarrow 0)}$, $R_{(8\rightarrow 7)/(1\rightarrow 0)}$, and $R_{(15\rightarrow 14)/(1\rightarrow 0)}$. Distributions for those models classified as starbursts are shaded with right-leaning (red) lines, while those of the failed models are shaded with left-leaning (blue) lines. The average ratios for all of the models analyzed here, as well as for the starburst and failed classes separately, can be found in Table 3. First, as expected from Sect. 3.1, Table 3 shows that the average brightness temperature ratios for the starburst models are considerably higher in magnitude than those of the failed models, indicating that the models containing an obscuring parsec-scale starburst possess a much higher excitation of CO lines than those that fail to meet this requirement. There is also an increasing separation between the distributions of the two classes as one analyzes the $R_{(3\rightarrow 2)/(1\rightarrow 0)}$, $R_{(6\rightarrow 5)/(1\rightarrow 0)}$, and $R_{(8\rightarrow 7)/(1\rightarrow 0)}$ histograms in sequence. This distinguishing feature allows for the possibility that temperature ratios could be used to search for obscuring parsec-scale starburst regions, if these regions can be resolved within their host galaxies. Finally, note that absorption is seen in most models for transitions with J_{Upper} greater than or equal to approximately 10. As can be seen in the histogram for $R_{(15\rightarrow 14)/(1\rightarrow 0)}$, and expected from Sect. 3.1, starburst models tend to have stronger absorption (i.e. more negative temperature ratios). This feature is even more apparent for lines with J_{Upper} somewhat lower than 15, such as the ratio of the $J = 13 \rightarrow 12$ line to the $J = 1 \rightarrow 0$ line.

3.3. Comparison to Observed CO SLEDs

Figure 3 shows luminosity SLEDs for two of the eighteen models analyzed in this work. The starburst model is marked by a black, solid line, while the failed model is depicted by a black, dotted line. The input parameters of both models are identified in Table 2. The observed SLEDs of various galaxies are offered for comparison, including the inner 800 pc of the nearby starburst galaxy M82 (Sanders et al. 2003; Ward et al. 2003; Panuzzo et al. 2010; magenta, solid line with open squares), the nearby ULIRG Mrk 231 (van der Werf et al. 2010; red, long-dashed line with open pentagons), the nearest ULIRG Arp 220 (Rangwala et al. 2011; green, short-dashed line with open triangles), and the $z=2.958$ ULIRG HERMES J105751.1+573027 (Conley, et al. 2011; Scott et al. 2011; blue, dotted line with filled circles). Comparing the SLEDs of the two nuclear starburst disk models, one notes that the magnitudes of the luminosities are higher for the successful starburst model, while the failed model is generally less luminous. Also, the ratio of the luminosities of the higher lines to the lowest transition tend to be lower for the failed models than for the starburst models,

indicating a more substantive excitation in the successful parsec-scale starburst models (see also Sect. 3.1, Figure 2 and Table 3). Lastly, note that the failed model falls into absorption (i.e. its luminosity SLED ends) at a lower J_{Upper} value than the starburst model.

The line luminosities estimated in this work are comparable to those reported in the literature if the size of the emission region is taken into account. The disk model of Thompson et al. (2005) was developed to describe LIRGs, ULIRGs, and other extreme starburst environments, and, thus, we compare our emission luminosities to observations for these objects, in addition to quasars and AGNs. Several reports in the literature on ULIRGs and quasar host galaxies find CO line luminosities for the $J = 1 \rightarrow 0$ transition in the range of $10^9\text{--}11$ K km s⁻¹ pc² (e.g. Chapman et al. 2008; Braun et al. 2011; Riechers 2011; Riechers et al. 2011; Scott et al. 2011; Wang et al. 2011). In particular, the work of Smolčić & Riechers (2011) describes observations of CO line emission of various nearby ($z \leq 0.1$) AGN. The values reported in Table 3 of Smolčić & Riechers (2011) track the range of CO line luminosities found in this work for the lowest lines. Therefore, the magnitude of the luminosities found in this work seems reasonable. One may also compare the luminosities of the models produced here to those of the observed galaxies given in Figures 3. This comparison sustains our previous conclusion that the models are an order of magnitude or so less luminous because of their substantially smaller masses of emitting material. The fact that the emission of the host galaxy of the nuclear starburst disk could be comparable to or greater than the emission of the disk, itself, implies that the emission of the innermost regions of the galaxy may have to be isolated in order to observe them. However, the observations plotted in Figure 3 are from galaxies selected to have substantial star formation rates and be very luminous in CO and will not necessarily be representative of the galaxies that host obscured Seyferts at $z < 1$, which typically have much lower rates of star formation (e.g., Silverman et al. 2009; Pierce et al. 2011). It would be interesting to compare the predicted SLEDs against ones obtained from X-ray selected $z < 1$ AGNs.

For better relative comparisons of the shape of the model CO SLEDs to observations, Figure 4 presents normalized flux (top panel) and luminosity (bottom panel) SLEDs for the models and the galaxies shown in Figure 3. The CO luminosity SLEDs are converted to solar luminosities (Papadopolous et al. 2010a; eq. 5) and are normalized to the total infrared luminosity between 8 and 1000 μm . The calculation of the infrared luminosity for the starburst disk models is detailed in Ballantyne (2008). The starburst disk models and the observed galaxies seem to have similar luminosity SLEDs, when normalized to the total infrared luminosity, indicating that, for a given reservoir of dusty star-forming gas, the ultra-compact starbursts produce a similar amount of CO luminosity for $J_{\text{Upper}} \lesssim 9$. However, at higher values of J_{Upper} , the models predict absorption, which is not observed in the large-scale emission of star-forming galaxies.

The observed flux SLEDs (Fig 4; top) have a shape generally peaking in the range of $J = 6-8$ similar to the starburst model peak at $J= 6-7$, while the failed model reaches a maximum at approximately 5. In addition, the observed flux SLEDs tend to be flatter at high J_{Upper} than the SLEDs of the models, possibly indicating the presence of an X-ray dominated region (XDR; see, e.g., van der Werf et al. 2010). Feedback from X-ray heating is not included in our calculations, but we show in Section 4.4 that it would impact the very inner-most region of a starburst disk, which has the least impact on the shape of the CO SLED (Figure 1). Crucially, none of the observed flux SLEDs show any indication of falling into absorption at large J_{Upper} . As the predicted absorption feature is a natural outcome of the steep density and temperature gradients within the starburst (see Sect. 3.1) and would not be altered by a presence of a XDR, we conclude that the absorption portion of the SLED is the most obvious and important observational prediction of the model. However, as discussed below, careful observational strategies and techniques (e.g., stacking) will be required to search for this signature.

4. Discussion

4.1. The CO Emission from Nuclear Starburst Disks

This paper has explored the CO emission and absorption properties of the Ballantyne (2008) nuclear starburst disk model. Eighteen models, nine of which produced the crucial pc-scale starburst that can act as an obscuring torus, were examined in detail, and found to produce CO luminosities and SLEDs similar to other extragalactic sources (e.g., ULIRGs and starburst galaxies; see Figures 3 and 4). Moreover, the shape of the CO SLEDs of the nuclear starburst disks are sensitive to the presence or absence of the pc-scale starburst (Figures 2, 3, and 4 and Table 3) with many of the predicted brightness temperature ratio differences exceeding 15% depending on the existence of the pc-scale burst. Therefore, if the nuclear starburst CO emission can be distinguished from that produced by the host galaxy, the SLED will provide a direct test of the nuclear starburst model for obscuring $z < 1$ Seyferts and provide help in understanding the coincidence of the peaks of the distribution of obscured AGNs and the star formation history around $z \sim 1$ (e.g. Tozzi et al. 2001; Barger et al. 2002; Hopkins 2004; Barger et al. 2005; Ballantyne 2008).

A potentially vital observational signature of the ultra-compact starburst model SLEDs shown in Figures 1 and 4 is the occurrence of absorption in the highest transitions. If confirmed, this absorption would be a characteristic feature of nuclear starburst disks (see Sect. 3.1); however, its possible that this feature may be altered by X-ray heating by the AGN. For example, Figure 4 shows an enhancement in the highest CO lines of Mrk 231,

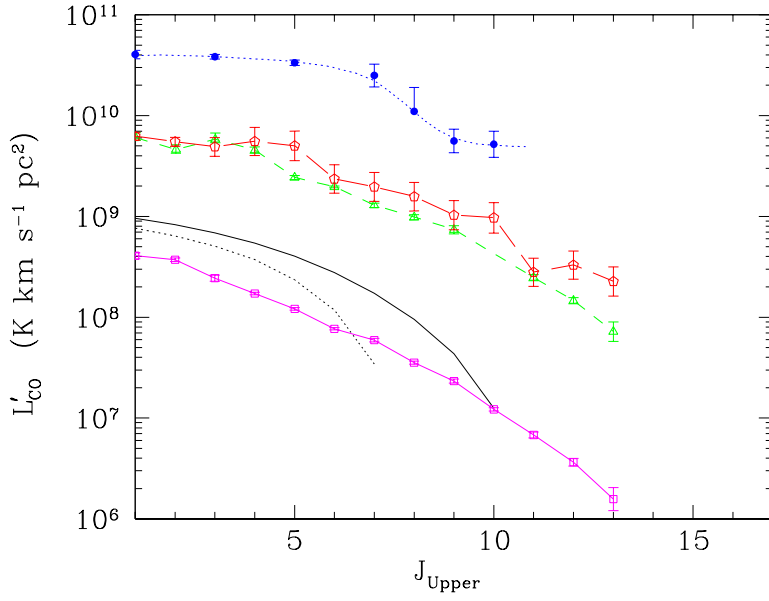


Fig. 3.— Plot of CO luminosity SLEDs for a starburst and a failed model, both of which are identified in Table 2. The starburst model is marked by a black, solid line, while the model without a parsec-scale obscuring starburst is marked by a black, dotted line. The CO SLED of the inner 800 pc of M82, a nearby starburst galaxy, is marked by solid, magenta line with open, square markers (Sanders et al. 2003; Ward et al. 2003; Panuzzo et al. 2010). Mrk 231, a nearby ULIRG, is depicted by a red, long-dashed line with open, pentagonal markers (van der Werf, et al. 2010). The nearest ULIRG Arp 220 is plotted with a green, short-dashed line and open, triangular markers (Rangwala, et al. 2011). Lastly, a distant ($z = 2.958$) ULIRG HERMES J105751.1+573027 is marked by a blue, dotted line with filled, circular markers (Conley et al. 2011; Scott et al. 2011).

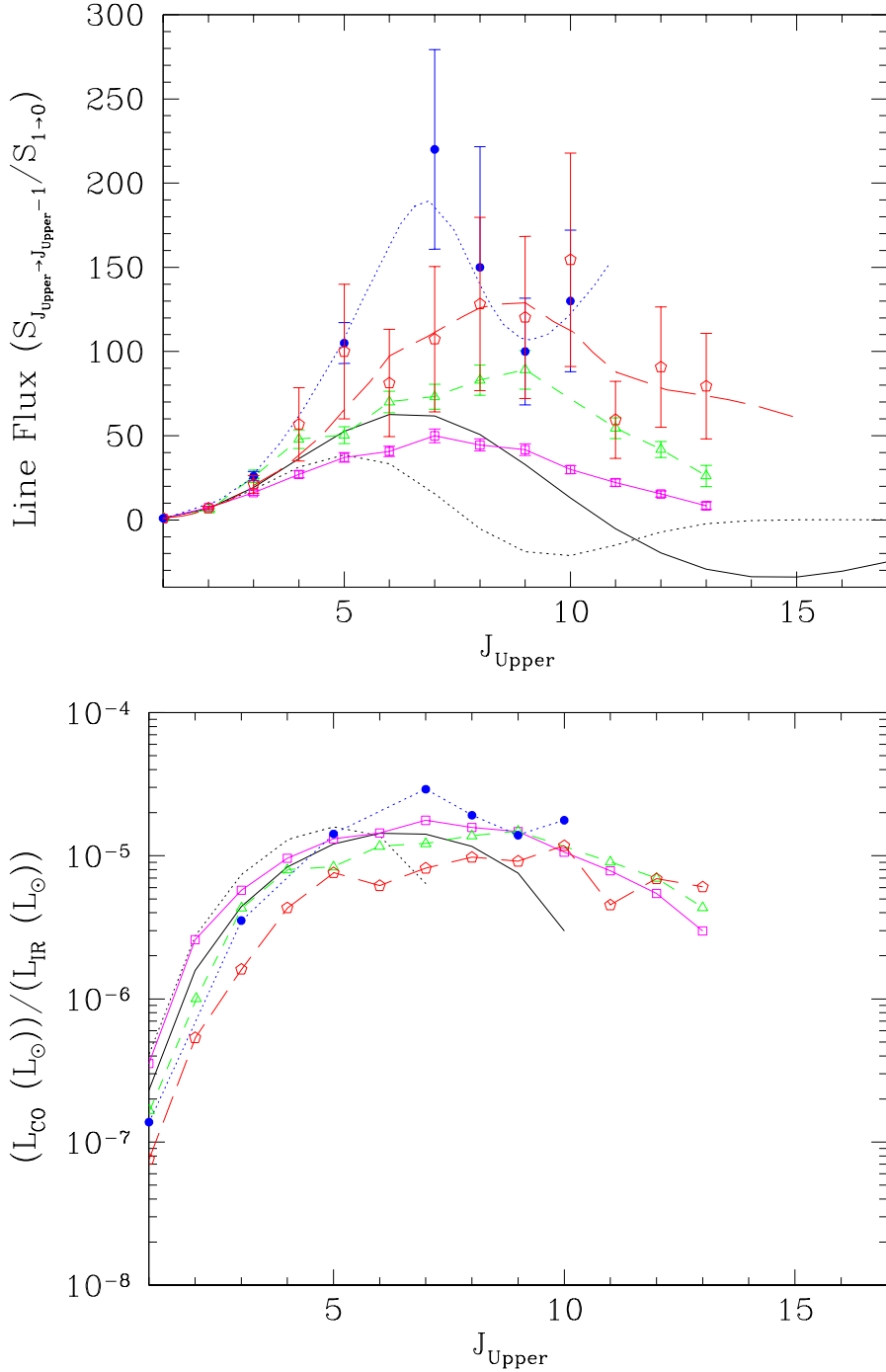


Fig. 4.— (Top) Plot of the CO flux SLEDs for a starburst and a failed model, both of which are identified in Table 2, as well as the observed SLEDs for several galaxies. The distributions are normalized by the flux of the lowest ($J = 1 \rightarrow 0$) transition. (Bottom) Plot of CO luminosity SLEDs, normalized by the total infrared luminosity (8-1000 μm), for the models and observed galaxies depicted in the other panel, as well as Figure 3. All luminosities are in solar units. The identification and marking scheme of the plot is identical to that of Figure 3.

Table 2. Model Input Parameters

$\frac{M_{BH}}{M_{\odot}}$	d_{dtg}	m	R_{out} (pc)	f_{gas}	Model Class
7.5	5.0	0.0750	250	0.10	f
7.5	5.0	0.0750	250	0.90	sb
7.5	10.0	0.0750	250	0.50	sb
7.5	5.0	0.0100	250	0.50	f
7.5	5.0	0.0250	250	0.50	f
7.5	5.0	0.1000	250	0.50	sb
7.5	1.0	0.0750	150	0.50	f
7.5	1.0	0.0750	200	0.50	f
7.0	5.0	0.0750	250	0.50	f
8.0	5.0	0.0750	250	0.50	sb
8.5	5.0	0.0750	250	0.50	sb
7.5	1.0	0.0750	250	0.50	f
7.5	5.0	0.0075	250	0.50	f
7.5	1.0	0.0750	50	0.50	sb
7.5	5.0	0.0500	250	0.90	sb
8.0	5.0	0.0075	50	0.90	sb
7.5	5.0	0.2000	250	0.50	sb*
7.5	5.0	0.0500	250	0.50	f*

Note. — Presented here are the input parameters and classifications for the eighteen models analyzed in this work. The models shown in Figures 1, 3 and 4 are indicated with asterisks. Lastly, the model class f stands for failed, which indicates that the model in question does not contain a parsec-scale obscuring starburst, and sb represents starburst, which is used to label all models that meet the starburst criteria of Section 2.1.

which are believed to result from the influence of an AGN-powered XDR (van der Werf et al. 2011). The possible effects of X-ray heating on the calculated SLEDs are discussed further below.

4.2. Comparisons with Previous Work

Wada & Norman (2002) investigated three-dimensional, time-dependent hydrodynamical simulations of a star-forming disk of material around a central supermassive black hole where turbulent velocities generated by supernova explosions provide the vertical support for the flared torus of obscuring material (see also Wada et al. 2009). Pérez-Beaupuits et al. (2011) present predictions for the relationship between CO luminosity and molecular mass in this scenario, but do not present integrated flux and/or luminosity SLEDs for the disk that could be compared with our results. However, it is clear that the two approaches are complimentary with the high resolution modeling of the Pérez-Beaupuits et al. (2011) simulations valuable for comparison to observations of nearby galaxies, while the work presented here with its results, which are integrated over frequency and space, is of more value for poorly resolved and more distant AGN host galaxies.

4.3. Detecting Nuclear Starbursts Around AGN

As shown in Sect. 3, the nuclear starburst disks predict CO luminosities large enough that these objects should be detectable by current instruments. However, if the host galaxy is also undergoing significant star-formation, the larger gas mass in the galaxy will produce a CO SLED that could swamp the one from the nucleus (Figures 3 and 4). One way to mitigate this problem is to directly resolve the nuclear starburst disk, requiring an angular resolution sufficient to resolve linear distances of ~ 100 pc at $z \lesssim 1$. The needed resolution may be possible for certain objects with the fully operational ALMA in the most extended configuration with a maximum baseline of 16 km. If one places the most luminous of the 18 starburst disks treated here (one with a successful pc-scale starburst) at $z = 0.3$, the $J = 3 \rightarrow 2$, $J = 4 \rightarrow 3$, and $J = 5 \rightarrow 4$ lines exceed the 1σ sensitivity limit of ALMA and will be imaged with angular resolutions that correspond to linear distances of a few tens of parsecs. If this source is at $z = 0.2$, the $J = 2 \rightarrow 1$ and $J = 3 \rightarrow 2$ lines are greater than the 3σ limit and may be resolved with an angular resolution of a few tens of parsecs. The $J = 5 \rightarrow 4$ line rises above the 5σ sensitivity limit at $z = 0.2$, while maintaining a linear resolution of approximately 32 parsecs, and the $J = 1 \rightarrow 0$ and $J = 7 \rightarrow 6$ lines exceed the 1σ sensitivity limit. Finally, at $z = 0.1$, the transitions from $J = 1 \rightarrow 0$ to $J = 4 \rightarrow 3$ are

all greater than the 6σ detection limit with angular resolutions in the tens of parsecs range, and the $J = 6 \rightarrow 5$ and $J = 8 \rightarrow 7$ lines exceed the 8σ limit.

For AGNs at $z \gtrsim 0.3$, many of the challenges in directly detecting a nuclear starburst disk could be overcome by leveraging information from other wavelengths, such as selecting a sample of AGNs with high-resolution radio imaging or mid-infrared colors that have low to weak galactic-scale star formation. The nuclear starburst disks would be expected to dominate the CO SLEDs of these galaxies. To illustrate this, Figure 5 plots the CO SLED of the Milky Way as measured by Fixsen et al. (1999) (green solid line), plus the previously discussed starburst disk SLEDs from Figures 3 and 4. Adding the Milky Way and the ultra-compact starburst SLED yields the solid black line, while the sum of the Milky Way and the failed model gives the SLED shown by the dotted black line. Thus, for galaxies with galactic-scale star-formation rates similar to those of the Milky Way, the presence of a nuclear starburst disk would dominate the observed CO SLED for $J_{\text{Upper}} \lesssim 8$. As discussed in Sect. 3.1, the predicted absorption at higher values of J_{Upper} is a direct consequence of the structure of the compact starburst disk, and we expect that this feature will be similarly dominant when observed against the background of a weakly starforming galaxy. Figure 5 also indicates that stacking of CO SLEDs from a sample of $z \lesssim 1$ X-ray selected AGNs will be a useful strategy to pull out the tell-tale signatures of the nuclear starburst disk.

4.4. The Effects of X-ray Dominated Regions

As mentioned above, the current calculations do not include the effects of X-ray heating by the AGN on the CO SLED. XDRs have been shown in simulations to produce substantial excitation of CO lines out to very high J values. The value of J_{Upper} at which the flux SLEDs peak for XDR models can be considerably greater than 10 (Schleicher et al. 2010), which is not observed for the nuclear starburst disk models explored here (see Figure 4). The size of the XDR at the inner radius of the nuclear starburst disk will depend on the density of the disk, the strength of the X-ray illumination by the central AGN, and the strength of the starburst in the disk (although this is a weak dependence). Schleicher et al. (2010) recently modeled the sizes of XDRs in starbursts near AGNs assuming typical AGN X-ray luminosities and ISM densities. The densities of the nuclear starbursts models are very large ($> 10^7 \text{ cm}^{-3}$ for a failed model and $> 10^9 \text{ cm}^{-3}$ for one with a pc-scale starburst), in which case figure 2 of Schleicher et al. (2010) indicates that the radius of the XDR would likely be only a fraction of a parsec for a disk with a pc-scale burst, while the XDR may extend $\sim 1 \text{ pc}$ for the failed model. If this is accurate then the strong absorption seen in the high J lines of the pc-scale starburst models (e.g., Figure 4) is robust to the inclusion of X-ray heating

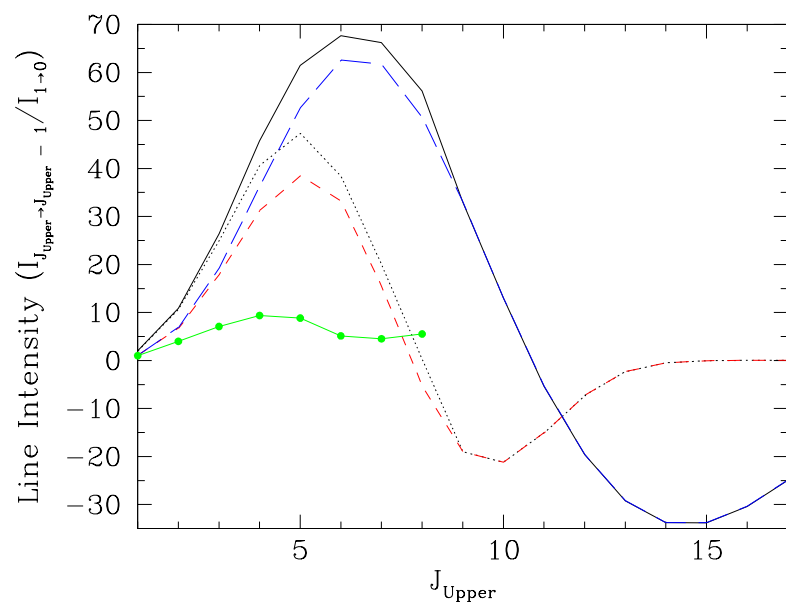


Fig. 5.— Plot of the normalized CO intensity SLED for the Milky Way (solid green line; Fixsen et al. 1999) and the starburst (blue, long-dashed line) and failed (red, short-dashed line) models shown in Figure 4. The sum of the Milky Way and starburst SLED yields the solid black line, while adding together the Milky Way and the failed starburst gives the dotted black line that peaks at lower J_{Upper} values and has a shallower absorption feature than that of the starburst.

because the absorption is caused by the material in the outer regions of the starforming disk (Fig. 1). The influence of AGN feedback and its effects on the calculated CO SLED will be included self-consistently in future work.

5. Conclusions

Nuclear starburst disks are an important potential mechanism to explain the obscuration of $z < 1$ Seyfert galaxies (Ballantyne 2008). A pc-scale starburst within the disk can potentially inflate the disk to the point where it obscures a large fraction of the lines-of-sight to the AGN and, thus, provides the toroidal obscuration required by the unified model. At the same time, the disk processes gas and moves it toward the central engine where it can accrete onto the black hole. The nuclear starburst disk therefore connects the black hole and galactic environments, a mechanism necessary to explain the observed relationships between black holes and their host galaxies. Observational tests of the presence of these disks are, therefore, important to verify the validity of the theory and to characterize the properties of these nuclear starburst disks (Pierce et al. 2011).

Here, we present the predicted CO line emission and absorption properties of nuclear starburst disks around AGN based on the analytic model of Ballantyne (2008). The CO luminosities and flux SLEDs are found to have quantitative and qualitative features similar to ULIRGs, LIRGs, and other starburst environments, but with smaller amplitudes due to the more compact sizes of the starbursts. Direct detection of the nuclear starburst will require significant sensitivity and resolution to separate its emission from the surrounding galaxy. Selecting a target sample of AGN galaxies with weak on-going galactic-scale star formation (which may be common for $z < 1$ X-ray AGNs; Silverman et al. 2009) will increase the likelihood of detection. Stacking of the CO SLEDs from such a sample will be an excellent method to measure the shape of the SLED out to large J_{Upper} .

Once detected, the CO flux SLEDs contain significant diagnostic information about the starburst disk. For example, starburst disks in which a parsec-scale starburst occurred are found to have larger brightness temperature ratios between the higher and lower lines, when compared to the ratios of the models that failed to meet this criterion (see Table 3 and Figure 2). The finding that an obscuring torus composed of a nuclear starburst disk should have a characteristic CO SLED shape is of particular interest, as it could provide an observational test to discern the structure of the nuclear regions of active galaxies. In addition, the large densities and temperatures, as well as steep radial gradients of these variables, associated with the pc-scale starburst produce a CO SLED that drops into absorption for $J_{\text{Upper}} > 10$. This prediction is robust to the presence of a XDR for typical Seyfert X-ray luminosities and

would be a clear indication of the ultra-compact nature of the nuclear starburst.

This work was supported in part by NSF award AST 1008067 to DRB. The authors thank D. Narayanan and N. Murray for useful discussions, and the anonymous referee for very useful comments that improved the paper.

REFERENCES

- Akylas, A., Georgantopoulos, I., Georgakakis, A., Kitsionas, S. & Hatziminaoglou, E., 2006, *A&A*, 459, 693
- Antonucci, R.R.J. & Miller, J.S. 1985, *ApJ*, 297, 621
- Antonucci, R.R.J. 1993, *ARA&A*, 31, 473
- Ballantyne, D.R., Everett, J.E. & Murray, N., 2006, *ApJ*, 639, 740
- Ballantyne, D.R. 2008, *ApJ*, 685, 787
- Barger, A.J., Cowie, L.L., Brandt, W.N., Capak, P., Garmire, G.P., Hornschemeier, A.E., Steffen, A.T., & Wehner, E.H. 2002, *AJ*, 124, 1839
- Barger, A.J., Cowie, L.L., Mushotzky, R.F., Yang, Y., Wang, W.-H., Steffen, A.T., & Capak, P. 2005, *AJ*, 129, 578
- Braun, R., Popping, A., Brooks, K., & Combes, F. 2011, *MNRAS*, 416, 2600
- Cazaux, S. & Tielens, A.G.G.M. 2004, *ApJ*, 604, 222
- Chapman, S.C., Neri, R., Bertoldi, F., Smail, I., Greve, T.R., Trethewey, D., Blain, A.W., Cox, P., Genzel, R., Ivison, R.J., Kovacs, A., Omont, A., & Swinbank, A.M. 2008, *ApJ*, 689, 889
- Conley et al. 2011, *ApJ*, 732, L35
- Dickman, R.L., Snell, R.L., & Schloerb, F.P. 1986, *ApJ*, 309, 326
- Draine, B.T. & Lee, H.M. 1984, *ApJ*, 285, 89
- Draper, A.R. & Ballantyne, D.R., 2010, *ApJ*, 715, L99
- Draper, A.R. & Ballantyne, D.R., 2011, *ApJ*, 740, 57

- Ferrarese, L. & Merritt, D. 2000, *ApJ*, 539, L9
- Fixsen, D.J., Bennett, C.L., & Mather, J.C. 1999, *ApJ*, 526, 207
- Fukui, Y. & Kawamura, A. 2010, *ARA&A*, 48, 547
- Gebhardt, K. et al. 2000, *ApJ*, 539, L13
- Gnedin, Nickolay Y., Tassis, Konstantinos, & Kravtsov, Andrey V. 2009, *ApJ*, 697, 55
- Hasinger, G., 2008, *A&A*, 490, 905
- Hogerheijde, M.R. & van der Tak, F.F.S. 2000, *A&A*, 362, 697
- Hopkins, A.M. 2004, *ApJ*, 615, 209
- Hsieh, P.-Y., Matsushita, S., Lim, J., Kohno, K., & Sawada-Satoh, S. 2008, *ApJ*, 683, 70
- Klemperer, W. 2006, *PNAS*, 203, 33, 12232-12234
- La Franca, F. et al., 2005, *ApJ*, 635, 864
- Lynden-Bell, D. 1969, *Nature*, 223, 690
- Maiolino, R. & Rieke, G.H. 1995, *ApJ*, 454, 95
- Panuzzo, P. et al. 2010. *A&A*, 518, L37
- Papadopoulos, P.P., Isaak, K., & van der Werf, P. 2010b, *ApJ*, 711, 757
- Papadopoulos, P.P., van der Werf, P., Isaak, K., & Xilouris, E.M. 2010a, *ApJ*, 715, 775
- Pelupessy, F.I., Papadopoulos, P.P., & van der Werf, P. 2006, *ApJ*, 645, 1024
- Pérez-Beaupuits, J.P., Wada, K., & Spaans, M. 2011, *ApJ*, 730, 48
- Pierce, C.M., Ballantyne, D.R., & Ivison, R.J. 2011, *ApJ*, 742, 45
- Pollack, J.B., Hollenbach, D., Beckwith, S., Simonelli, D.P., Roush, T., & Fong, W. 1994, *ApJ*, 421, 615
- Rangwala, N. et al. 2011, *ApJ*, 743, 94
- Riechers, D.A. 2011, *ApJ*, 730, 2, 108
- Riechers, D.A., Carilli, C.L., Maddalena, R.J., Hodge, J., Harris, A.I., Baker, A.J., Walter, F., Wagg, J., Vanden Bout, P.A., Weiss, A., & Sharon, C.E. 2011, *ApJ*, 739, L32

- Risaliti, G., Elvis, M., Bianchi, S. & Matt, G., 2010, MNRAS, 406, L20
- Sanders, D.B., Mazzarella, J.M., Kim, D.-C., Surace, J.A., & Soifer, B.T. 2003. AJ, 126, 1607
- Sault, R.J., Teuben, P.J., & Wright, M.C.H. 1995. "A retrospective view of Miriad" In *Astronomical Data Analysis Software and Systems IV*. ed. Shaw, R., Payne, H.E., & Hayes, J.J.E. ASP Conference Series, 77, 433-436
- Schieven, G., ed. 2011, Observing with ALMA: A Primer for Early Science, ALMA Doc 0.1, ver 2.2
- Schleicher, D.R.G., Spaans, M., & Klessen, R.S. 2010, A&A, 513, A7
- Schruba, A. et al. 2011, ApJ, 142, 37
- Scott, K.S. et al. 2011, ApJ, 733, 1, 29
- Scoville, N.Z., Sargent, A.I., Sanders, D.B., & Soifer, B.T. 1991, ApJ, 366, L5
- Semenov, D., Henning, T., Helling, C., Ilgner, M., & Sedlmayr, E. 2003, A&A, 410, 611
- Shakura, N.I. & Sunyaev, R.A. 1973, A&A, 24, 337
- Silverman, J.D., Lamareille, F., Maier, C., Lilly, S.J., Mainieri, V. et al. 2009, ApJ, 696, 396
- Simpson, C., 2005, MNRAS, 360, 565
- Smolčić, V. & Riechers, D.A. 2011, ApJ, 730, 2, 64
- Solomon, P.M. & Vanden Bout, P.A. 2005, ARA&A, 43, 677
- Solomon, P.M. & Wickramasinghe, N.C. 1969, ApJ, 158, 449
- Spergel, D.N. et al. 2003, ApJS, 148, 175
- Spergel, D.N. et al. 2007, ApJS, 170, 377
- Thompson, T.A., Quataert, E., & Murray, N. 2005, ApJ, 630, 167
- Tozzi, P. et al. 2001, ApJ, 562, 42
- Treister, E. & Urry, C.M., 2006, ApJ, 360, 115
- Treister, E., Krolik, J.H. & Dullemond, C., 2008, ApJ, 679, 140

- Tremaine, S., et al. 2002, ApJ, 574, 740
- Tueller, J., Mushotzky, R.F., Barthelmy, S., Cannizzo, J.K., Gehrels, N., Markwardt, C.B., Skinner, G.K. & Winter, L.M., 2008, ApJ, 681, 113
- Ueda, Y., Akiyama, M., Ohta, K. & Miyaji, T., 2003, ApJ, 598, 886
- van der Werf, P.P. et al. 2010, A&A, 518, L42
- Vila Vilaro, B. 2011, ALMA Cycle 0 Technical Handbook, Version 1.0, ALMA
- Wada, K. & Norman, C.A. 2002, ApJ, 566, L21-L24
- Wada, K., Papadopoulos, P.P., & Spaans, M. 2009, ApJ, 702, 63
- Wang, R. et al. 2011, ApJ, 739, L34
- Ward, J.S., Zmuidzinas, J., Harris, A.I., & Isaak, K.G. 2003, ApJ, 587, 171
- Xue, Y.Q., Brandt, W.N., Luo, B., Rafferty, D.A., Alexander, D.M., et al., 2011, ApJ, 720, 368
- Young, J.S. & Scoville, N.Z. 1991, ARA&A, 29, 581

Table 3. Brightness Temperature Ratios

Model Type	$R(\frac{3 \rightarrow 2}{1 \rightarrow 0})$	$R(\frac{6 \rightarrow 5}{1 \rightarrow 0})$	$R(\frac{6 \rightarrow 5}{3 \rightarrow 2})$	$R(\frac{8 \rightarrow 7}{1 \rightarrow 0})$	$R(\frac{15 \rightarrow 14}{1 \rightarrow 0})$
failed	0.66	0.15	0.23	-1.0×10^{-2}	-2.6×10^{-5}
starburst	0.71	0.29	0.41	0.10	-1.0×10^{-2}
Averages					
$\langle \text{total} \rangle$	0.73	0.27	0.35	7.6×10^{-2}	-2.9×10^{-2}
$\langle \text{starburst} \rangle$	0.78	0.37	0.45	0.15	-5.7×10^{-2}
$\langle \text{failed} \rangle$	0.68	0.17	0.24	9.7×10^{-4}	-5.4×10^{-4}

Note. — Shown here are brightness temperature ratios for the models in Figures 3 and 4, as well as average ratios for all eighteen tested models, all of the successful starburst models, and the models that failed to achieve a starburst. Note that the starburst ratios are significantly higher than those of the failed models, particularly when considering higher-J lines.